

# Typical Profiles and Distributions of Plasma and Magnetic Field Parameters in Magnetic Clouds at 1 AU

L. Rodriguez<sup>1</sup>, J. J. Masías-Meza<sup>2</sup>, S. Dasso<sup>3,4</sup>, P. Démoulin<sup>5</sup>, A. N. Zhukov<sup>1,6</sup>, A. Gulisano<sup>2,3,7</sup>, M. Mierla<sup>1,8</sup>, E. Kilpua<sup>9</sup>, M. West<sup>1</sup>, D. Lacatus<sup>8,10</sup>, A. Paraschiv<sup>8,10</sup>, M. Janvier<sup>11</sup>

<sup>1</sup> *SIDC, Royal Observatory of Belgium, STCE, Brussels, Belgium*

<sup>2</sup> *Departamento de Física (FCEN-UBA-IFIBA), Buenos Aires, Argentina*

<sup>3</sup> *Instituto de Astronomía y Física del Espacio (UBA-CONICET), Buenos Aires, Argentina*

<sup>4</sup> *Departamento de Ciencias de la Atmósfera y los Océanos and Departamento de Física (FCEN-UBA), Buenos Aires, Argentina*

<sup>5</sup> *Observatoire de Paris, LESIA, UMR 8109 (CNRS), F-92195 Meudon Principal Cedex, France*

<sup>6</sup> *Skobeltsyn Institute of Nuclear Physics, Moscow State University, 119992 Moscow, Russia*

<sup>7</sup> *Instituto Antártico Argentino, Buenos Aires, Argentina*

<sup>8</sup> *Institute of Geodynamics of the Romanian Academy, Jean-Louis Calderon 19-21, 020032 Bucharest-37, Romania*

<sup>9</sup> *Department of Physics, Division of Geophysics and Astronomy, University of Helsinki, Helsinki, Finland*

<sup>10</sup> *School of Mathematical Sciences, Monash University, Clayton, Victoria 3800, Australia*

<sup>11</sup> *Institut d'Astrophysique Spatiale, UMR8617, Univ. Paris-Sud-CNRS, Université Paris-Saclay, Batiment 121, 91405 Orsay Cedex, France*

## Abstract

Magnetic clouds (MCs) are a subset of interplanetary coronal mass ejections (ICMEs). They are important due to their simple internal magnetic field configuration, which resembles a magnetic flux rope, and because they represent one of the most geoeffective types of solar transients. In this study, we analyze their internal structure using a superposed epoch method on 63 events observed at L1 by ACE, between 1998 and 2006. In this way, we obtain an average profile for each plasma and magnetic field parameter at each point of the cloud. Furthermore, we take a fixed time window upstream and downstream from the MC, in order to sample also the regions preceding the cloud and the wake trailing it. We then perform a detailed analysis of the internal characteristics of the clouds, and their surrounding solar wind environments. We find that the parameters studied are compatible with log-normal distribution functions. The plasma beta and the level of fluctuations in the magnetic field vector are the best parameters to define the boundaries of clouds. We find that in one third of the events, there is a peak in plasma density close to the trailing edge of

the flux ropes. We provide several possible explanations for this result and investigate if the density peak is of a solar origin (e.g. erupting prominence material) or formed during the magnetic cloud travel from the Sun to 1 AU. The most plausible explanation is the compression due to a fast overtaking flow, coming from a coronal hole located to the east of the solar source region of the magnetic cloud.

## 1. Introduction

Coronal Mass Ejections (CMEs) are large-scale solar eruptive events, in which large amounts of plasma carrying magnetic flux and helicity (see *e.g.* Démoulin et al., 2015, and references therein) are expelled into the interplanetary space. When sampled *in situ* by a spacecraft in the interplanetary medium, they are called Interplanetary CMEs (ICMEs). Magnetic clouds (MCs) are an important subset of ICMEs, which exhibit a particular internal magnetic field configuration resembling that of a flux rope. This is characterized by enhanced magnetic field intensity, smooth rotation of its magnetic field vector and low temperature (*e.g.* Burlaga, 1991).

The classical three-part structure of a CME (bright front, dark cavity, and dense core) is usually also interpreted in terms of a magnetic flux rope propagating in the corona (see *e.g.* Illing and Hundhausen, 1986; Vourlidas et al., 2013). The bright front corresponds to the plasma pile-up in front of the flux rope, the cavity represents the bulk of the flux rope, and the dense core is the erupting prominence that is located in the bottom (concave-out) parts of the flux rope field lines. As coronagraphic white-light observations of CMEs are only sensitive to the coronal electron density (weighted depending on the distance with respect to the plane of the sky, see *e.g.* Billings, 1966), a possible method to identify the correspondence between CME and ICME structures is the investigation of density structures *in situ*. However, it is very difficult to identify the corresponding three-part morphology in ICMEs detected *in situ* (*e.g.* Kilpua et al., 2013a). For fast ICMEs, one usually detects a fast forward shock driven by the magnetic cloud, and dense plasma in the sheath between the shock and the cloud which is caused by the plasma pile-up. A link between CMEs and ICMEs can be established using heliospheric imaging that can track CME density structures all the way from the solar corona to 1 AU (Howard et al., 2008; Davis et al., 2009), or by combining observations with modelling (Rodriguez et al., 2011). Möstl et al. (2009) investigated two CME-ICME pairs and found that the CME bright front corresponds to the post-shock sheath in front of the cloud, and the dense CME core corresponds to the density enhancement in the trailing part of the magnetic cloud. However, the CME-driven shock wave observed in coronagraph images (see *e.g.* Ontiveros and Vourlidas, 2009) travels ahead of the classic bright frontal structure (Vourlidas et al., 2013). Thus two dense structures corresponding to the shock and to the bright front are expected to be observed ahead of the magnetic cloud, which is not the case. Similarly, a dense structure at the trailing end of interplanetary flux

ropes is not detected systematically. Lepping et al. (2003) studied 19 MCs observed from 1995 to 1998 and created profiles of the plasma and magnetic field parameters in them. They found a density increase towards the end of the cloud in half of the cases (see their Figures 3 and 4). Lynch et al. (2003) presented a study of 56 MCs observed between 1998 and 2001. They divided their observations into fast and slow clouds, which exhibited different plasma characteristics and composition, but the trailing density peaks were not observed in either population. Unusual charge states (*e.g.* He<sup>+</sup> ions) are usually interpreted as traces of the cold prominence plasma (Schwenn et al., 1980; Lepri et al., 2010). However, ions with unusual charge states are very rarely identified *in situ*, so erupting prominence plasma is typically not found in ICME observations (*e.g.* Lepri et al., 2014). In general, the correspondence between the coronal and interplanetary structures in CME-ICME events remains unclear.

The primary motivation of the current work is to construct the typical profiles of the main plasma and magnetic field properties within magnetic clouds and in their immediate surroundings, using a large sample of events observed in different phases of the solar cycle. As stated by Kilpua et al. (2013b), defining magnetic cloud boundaries is often very difficult and such generic profiles can be very valuable in providing context for interpreting individual observations and in general for studying the internal structure of magnetic clouds.

In particular, we focus on the plasma density profile within those clouds, for which we observe a density peak near their trailing edge. The information provided by these profiles is important for understanding the effect that an increase in density may have on the solar wind-magnetosphere coupling efficiency (both when connected to southward and northward IMF). Density in the solar wind correlates with the density of the plasma sheet in the Earth's magnetotail (*e.g.* Borovsky et al., 1998), which is the primary source of the storm-time ring current (*e.g.* Wang et al., 2008). During periods with a northward IMF, high density may lead to the formation of a super-dense plasma sheet, which later can increase the ring current (*e.g.* Lavraud et al., 2005). For example, the MC that arrived at the Earth on January 10, 1997 (Burlaga et al., 1998) contained a high-density peak in its tail that led to significant geomagnetic effects and severely damaged the U.S. Telstar 401 satellite (Reeves et al., 1998). For that case, the peak in density was related to prominence material, which is one of the possible explanations for the peaks observed in the present study. The trailing density peak could also result from the dynamics of the MC transport from the Sun to the Earth, for example compression caused by a trailing fast solar wind stream, which could in turn lead to increased geoeffectiveness (Fenrich and Luhmann, 1998; Kilpua et al., 2012a). In this work, we present and analyse several possible explanations for such peaks observed in the tails of MCs.

Section 2 reports the data and the MCs used in this study. In Section 3 we describe the superposed epoch analysis and the methods used to obtain the typical MC profiles at 1 AU. Section 4 presents the analysis of the results and describes the observations of plasma

density enhancements in the trailing part of the MCs, which are investigated in more detail in Section 5. Finally, Section 6 provides a summary and conclusions of our work.

## 2. Data and Event Selection

In this study, the MCs are taken from the list of “Near-Earth Interplanetary Coronal Mass Ejections Since January 1996”, compiled by I. Richardson and H. Cane (R&C list hereon) available at <http://www.srl.caltech.edu/ACE/ASC/DATA/level3/icmetable2.htm> (Richardson and Cane, 2010). We use data from the ACE spacecraft for magnetic field and plasma data with 64-second cadence and the plasma composition data for oxygen charge states ( $O^{+7}/O^{+6}$ ) taken with 1-hour cadence. ACE was launched on August 25, 1997 and is currently operating close to the Lagrangian point L1 of the Sun-Earth system. The R&C list separates the MCs into three categories according to the quality of MC (this MC flag is located in column “L” in the catalogue). A flag of 2 indicates a clear MC, a ‘1’ signals a doubtful MC identification and a ‘0’ denotes that a MC is not detected within the ICME. Only clearly identified MCs (*i.e.* those with a quality flag ‘2’) are used in this work. Our list of events starts in February 1998 (with the start of availability of ACE plasma data) and finishes in December 2006 (last events with detailed MC information in the R&C list). Our final list contains a total of 63 MCs.

In order to find the solar counterpart of the magnetic clouds (*i.e.* CMEs) we used data from the Large Angle Spectroscopic Coronagraph (LASCO, see Brueckner et al., 1995) onboard the SOLar and Heliospheric Observatory (SOHO) spacecraft. The C2 and C3 coronagraphs of LASCO record the brightness of the white-light corona from 2.2 to 6 solar radii ( $R_s$ ) and from 3.7 to 32  $R_s$ , respectively. To identify the on-disc signatures of CMEs we used the data from the Extreme-ultraviolet Imaging Telescope (EIT, see Delaboudinière et al., 1995) onboard SOHO and/or  $H\alpha$  ground based observations (taken from <ftp://ftp.bbso.njit.edu/pub/archive/> that contains  $H\alpha$  observations from Big Bear Solar Observatory, Kanzelhoehe Solar Observatory and Yunnan Astronomical Observatory). EIT observes the solar atmosphere up to 1.5  $R_s$ , in a temperature range from  $6 \times 10^4$  to  $3 \times 10^6$  K at four different wavelengths: 30.4 nm, 17.1 nm, 19.5 nm and 28.4 nm.  $H\alpha$  images detect the emission of the cooler chromosphere at around 6000 K, where erupting filaments can be identified. An example CME is shown in Figure 1, with the eruption from source region NOAA AR 9866 visible in EIT (left panel) and the corresponding CME on LASCO C2 (right panel).

## 3. Superposed Epoch Method

In this study, the MCs are analysed by means of a superposed epoch analysis. This method is used to create an average profile of the MC plasma and magnetic field characteristics. To perform this analysis, we require each magnetic cloud to be recorded with an equal number of data points. This is normally not the case, since each cloud has a different duration. To remedy this, we determine a grid of 50 equally spaced bins inside each MC. All valid data points are averaged within each bin to build the average profile. If there is no data in a certain bin window, for a certain event, this event is then not counted in this bin. Moreover, if an original time series has data gaps in more than 20% of the MC structure, we discard it from the average profile.

The next step consists in averaging corresponding data points over all MCs, so data points 1 from each magnetic cloud will be averaged, followed by data points 2, and so on. We take the mean and the median value at each point taking into account the number of events that contribute in that bin. We include the median as it is less affected by extreme values in the distribution. In this manner, an average profile of all the MCs can be created, where each point has associated standard deviations for the distribution, the mean and the median value. This procedure is done for the magnetic field intensity, solar wind speed, proton temperature, proton number density, plasma beta, oxygen charge state ratio ( $O^{+7}/O^{+6}$ ), alpha-to-proton ratio, and the magnetic field vector variance.

Finally, we select a region in front of the MC with the same duration as the MC and a region with the double duration after the MC rear boundary. This choice was made to give sufficient time for the parameters to recover background solar wind levels. The region ahead of the MC will in some cases include passage of the shock and hence consist of both the sheath and upstream ambient solar wind. The MC boundaries correspond to the first and last point of the MC. All the regions are re-sampled with the same factor, in this way, we resampled each cloud to 50 points, plus 50 points before and 100 points after the event (200 points in total). The sheaths of the events analysed in this study are treated in detail by Masias-Meza et al. (2016).

## **4. Analysis of the Results**

### **4.1 Magnetic Field and Plasma Profiles**

Several characteristics of magnetic clouds and their environment can be deduced from the result of the superposed epoch analysis. Figure 2 shows the profiles of magnetic field and plasma parameters in and around selected events created using the procedure described in Section 3. Each plot was created by applying the superposed epoch method to 63 MCs. MC periods are marked by the blue areas. Error bars (in grey) represent the standard deviations of the mean (black curve), and the red curve is the median.

Firstly, the magnetic field magnitude is found to peak inside the cloud, reaching values twice as large as those found in the ambient solar wind (as can be seen from panel (a) of Figure 2). Also, the peak is asymmetric towards the leading edge. The expansion of the MC is typically not enough to explain this asymmetry (see Démoulin et al., 2008, and their Figure 3), but this could be a consequence of the combined intrinsic spatial asymmetry within the flux rope, and its interaction with the surrounding solar wind (with a higher total pressure in the region preceding the flux rope).

Next, the proton density (panel (d)) and temperature (panel (c)) peak before the arrival of the flux rope and represent a clear signature of the compressed pile-up plasma region in front of the flux rope. The proton temperature then decreases and reaches a minimum in the MC region, which is also a consequence of the internal expansion (Gosling et al., 1973; Richardson and Cane, 1995). As mentioned in Section 1, the proton density peak observed close to the flux rope leading edge probably corresponds to the bright front of the associated CME observed by coronagraphs. The negative slope of the speed profile (panel (b)) marks the typical expansion of magnetic clouds (*e.g.* Klein and Burlaga, 1982; Gulisano et al., 2010). The plasma beta (panel (e)) is low within the clouds, meaning that these are magnetically dominated structures.

The profiles of temperature, density, plasma beta and the variation of the magnetic field vector (panel (c), (d) and (h)) as well as  $O^{+7}/O^{+6}$  (panel (f)) relative abundances have relatively flat profiles within the superposed MC (*i.e.* there are no big variations from the leading edge to the trailing part of the cloud). Proton density and plasma beta (panels (d) and (e)) have their minimum in the leading part of the cloud, while the temperature reaches its minimum towards the end of the cloud (but indeed the differences are not large within the cloud).

The variation of the magnetic field unit vector is denoted in Figure 2 (panel (h)) as rmsBoB (meaning the RMS of B over its magnitude), with its magnitude being the root-mean-square (RMS) value of the magnetic field vector over a 64 seconds window, normalized to the magnitude of the average magnetic field intensity in the same window (Equations 1 and 2).

$$rmsBoB(t) = rms(\mathbf{B}(t))/B(t) \quad (1)$$

$$rms(\mathbf{B}(t)) = \sqrt{\sum_{i=1}^3 \langle (B_i - \langle B_i \rangle)^2 \rangle} \quad (2)$$

This normalization is important because the absolute RMS is highly correlated to the magnitude of the average vector, and we are interested in seeing the intrinsic magnetic field variability along these structures. The magnetic field within the MC is found to vary very smoothly, and its normalized variation, rmsBoB, is a factor of 3 smaller than in the ambient solar wind. We also note the very narrow standard deviations from the mean value, and the similarities between the mean and median values, hinting at a more symmetric distribution compared to the other parameters. As a consequence, the magnetic field variation can be

considered as a very robust parameter for MC identification. Furthermore, together with the plasma beta, the variation of the magnetic field unit vector clearly marks the boundaries of the clouds. This confirms previous studies (e.g. Burlaga et al., 1981; Gosling, 1990). These features have an additional importance as the identification of the MC boundaries is a difficult issue (e.g. Dasso et al., 2006) and these two parameters can be very helpful when defining the limits between MCs and the surrounding solar wind. Our result is also in agreement with the work by Kilpua et al. (2013a), who showed that ultra-low-frequency fluctuations in the magnetic field components decrease dramatically at the ICME edges. Our quantity provides a useful quantitative background to measure the level of fluctuations in MCs.

## 4.2 Composition Profiles

The alpha-to-proton ratio profile is found to peak towards the end of the MCs (panel (g) of Figure 2), and takes longer to recover to its ambient solar wind values after the clouds have passed, which is in contrast to the rate with which the ratio rises in front of the clouds. This behavior was also observed by Richardson and Cane (2004), who suggested that an enhanced alpha-to-proton ratio is the result of helium gravitational settling. In a separate study, Manchester et al. (2014) simulated a very fast CME and, due to its deceleration, they found that the prominence material moved towards the front of the ICME. In contrast, the average alpha-to-proton ratio found here increases towards the end of the cloud. This could be a consequence of a reverse process: most MCs in this study are slow, and then a much weaker deceleration is experienced in the interplanetary medium while the gravitational settling would occur when they are accelerated in the corona. So the heavier ions would have more inertia and the tendency to accumulate at the rear, as suggested by Richardson and Cane (2004).

The relative ionization states of solar wind ions become constant, *i.e.* they “freeze-in”, at a few solar radii from the Sun (Hundhausen, 1968). Hence, at greater distances, the measurement of the charge states can be used as a proxy for inferring conditions close to the Sun, thus providing a link between interplanetary and conditions at a few solar radii from the Sun. Furthermore, charge states are the parameters least affected by propagation effects, because they are frozen-in, in contrast to density and temperature for example, that may be significantly affected by compression and expansion of the MC. The  $O^{+7}/O^{+6}$  shown in Figure 2 (panel (f)) is clearly increased within the MC, indicating high temperatures in the source region of the CME (Henke et al., 1998; Rodriguez et al., 2004; Song et al. 2015). This parameter provides a very good signature for identifying magnetic cloud material (see also Figure 8 of Richardson and Cane, 2004).

Both the charge states and the alpha-to-proton values take longer to reach background solar wind levels following the MC compared to the rate of their increase before the MC (panels (f) and (g) of Figure 2). This could be an indication of the presence of a long wake or back region following magnetic clouds, i.e. a region trailing the cloud where magnetic cloud and ambient solar wind plasmas mix. In contrast, the plasma and magnetic field parameters (panels (b), (c), (d) and (h)) do not show a clear ICME-related signature in this back region, consistent with the analysis in Section 5 of Richardson and Cane (2010). The plasma beta (panel (e)) is larger than unity, and the density (panel (d)) has nominal solar wind values (apart from a peak at the MC rear, see below). Also the level of fluctuations of the magnetic field vector (panel (h)) increases significantly after the MC with a transition region where it goes back to solar wind conditions. The magnetic field intensity and the temperature (panels (a) and (c)) have the most progressive transition from the MC to the typical solar wind conditions. All these features could be the consequence of the formation of a back region in magnetic clouds, due to reconnection of the flux rope with the surrounding solar wind (see Dasso et al., 2006, 2007; Ruffenach et al., 2015). This back region is a remnant part of the flux rope after its reconnection with the solar wind fields at the front of the magnetic cloud. The original composition is still present in this region. There,  $O^{+7}/O^{+6}$  and alpha-to-proton ratios are larger than the ambient solar wind values (panels (f) and (g) of figure 2). The flux rope plasma gets mixed with the solar wind plasma, as a consequence of reconnection (the collision time is long, so ions can travel along field lines). The mixing is expected to increase with time (from the reconnection time), so indeed the plasma further away from the MC rear boundary, that reconnected earlier, is expected to be more mixed with the solar wind, as observed in Figure 2.

In conclusion, the  $O^{+7}/O^{+6}$  and alpha-to-proton ratios are important parameters, not only for defining the flux rope extent as observed at 1 AU, but also for characterizing it when it was much closer to the Sun, before reconnection with the solar wind field started. Still the rear boundary of this extended flux rope is not well defined (no sharp transition). The interplanetary magnetic field magnitude has a similar property (*i.e.* it decreases gradually after the MC rear end to reach quiet solar wind values ), but with a slightly shorter tail than both  $O^{+7}/O^{+6}$  and alpha-to-proton ratio.

### 4.3 Distribution Functions of Plasma and Magnetic Field Parameters

In general there is a noticeable difference between mean and median values in the parameter profiles shown in Figure 2, and these differences are not the same inside and outside the MC. This indicates a non-symmetric distribution function for these parameters within MCs. One exception is seen in the panel of rmsBoB, the similarities between the mean and median values hint at a more symmetric distribution compared to the other parameters. As can be seen in the other panels, the mean values are higher than the

medians and thus the distributions are skewed to values larger than the mean values. This is in agreement with results of Guo et al. (2010) and Mitsakou and Moussas (2014), who found similar results related to ICME mean values. In their work it was shown how such ICME parameter distributions could be approximated by log-normal distribution functions. Burlaga et al. (1979, 1998) have found log normal distributions in solar wind plasma and magnetic field. In order to assess whether log-normal distributions are also found in magnetic clouds, we generated histograms of each of the parameters analyzed, inside MCs, and fitted them with the lognormal function as described by Equation 3:

$$f(x, \mu, \sigma) = \frac{1}{x\sigma\sqrt{2\pi}} e^{-(\ln(x)-\mu)^2/2\sigma^2} \quad (3)$$

where  $\mu$  and  $\sigma$  are the mean and standard deviation of the natural logarithm of variable  $x$  respectively.

The analysis is carried out over 16 points around the center of each cloud (33% of the points in each MC). The number of points was chosen as a compromise in order to properly sample the characteristics and homogeneous properties of the center of the cloud, while avoiding mixing the fluctuations of a global trend with boundary contamination. The observed distributions are binned in order to resolve the main peak and the shape of the distribution below and above the peak in a comparable manner. The bin number is limited to have enough cases in each bin around the maximum (typically above 40). With these constraints we try to optimize the representation of the observed distributions. The results are shown in Figure 3. Log-normal fits are included in the figure, with the corresponding parameters. The median value is indicated as a vertical dashed line, and a red band is shown between the percentiles ( $50 - 33/2 = 33.5\%$ ) and ( $50 + 33/2 = 66.5\%$ ). The 33% was chosen after an iterative process to represent correctly the core of the distribution.

We find that all quantities have distributions close to the fitted lognormal functions, with the velocity being the quantity that least resembles the fitted lognormal function. In Table 1, we compare the mean and median values with those obtained by Mitsakou and Moussas (2014) in a similar study of ICMEs. The mean magnetic field in MCs is larger than that in ICMEs, as it can be expected when crossing a flux rope. The average MC plasma beta and temperature are lower than in ICMEs, also expected results as a consequence of the presence of a flux rope in MCs.

Quantity	Median	Mean	Mean (ICME)
<b>B [nT]</b>	13.1	15.1	10.1

<b>V [km/s]</b>	456	488	467
<b>N<sub>p</sub> [cm<sup>-3</sup>]</b>	5.64	7.34	6.8
<b>T [10<sup>5</sup> K]</b>	0.25	0.54	0.76
<b>β</b>	0.22	0.32	0.84
<b>rmsBoB</b>	0.02	0.02	-
<b>O<sup>+7</sup>/O<sup>+6</sup></b>	0.68	0.93	-
<b>n<sub>α</sub>/n<sub>p</sub></b>	0.05	0.06	-

Table 1. Median (2<sup>nd</sup> column) and mean (3<sup>rd</sup> column) values of the different plasma and magnetic field parameters within magnetic clouds as calculated in this work. For comparison, the mean values for ICMEs are given in the 4<sup>th</sup> column (taken from Table 1 and 2 of Mitsakou and Moussas, 2014)

## 5. Origin of Density Peaks in the Trailing Edge of MCs

The results of the superposed epoch analysis in Figure 2 indicate that there is an enhancement in proton density at the rear boundary of the MC (panel (d) of Figure 2). The velocity panel of Figure 2 (panel (b)) also shows that there is typically a faster stream following the MC (*i.e.*, a clear peak of  $V_{sw}$  at around 1.3 in normalized time). This then motivates the questions: Is the observed peak in the proton density profile a consequence of dynamical processes that occurred during the MC transport from the Sun to the Earth (*i.e.* a fast solar wind stream that pushes the flux rope from behind)? Can it be generated by intrinsic processes related to the origin of the MCs in the low corona (*i.e.* pre-existing dense plasma resulting *e.g.* from prominence material as one can expect from observations of three-part CMEs, as shown by Möstl et al., 2009)?

Apart from compression from a high speed stream (HSS) and intrinsic processes at the Sun, flux rope expansion is yet another process that should be taken into account (see *e.g.* Gosling et al. 1998). This expansion would need to be stronger than the expansion required for pressure equilibrium with the surroundings (Démoulin and Dasso, 2009; Gulisano et al., 2010), so that it would exert a pressure on the adjacent solar wind, and could therefore produce the observed density increase. A priori, we could make a distinction between expansion and compression by looking at the location of the density peak: inside or outside

the flux rope boundary. Unfortunately, in practice it is not possible, because the uncertainty on the boundary location is larger than the precision needed to carry out a consistent analysis.

One should also consider that a combination of the processes described above could be acting together on the clouds, and may explain why some clouds exhibit multiple peaks. We explore the different explanations in the following subsections.

Following the analysis of the individual events, we find that in 22 out of 63 cases a peak in proton number density is found close to the trailing edge of the cloud. We consider only the peaks appearing within 30% of the cloud duration before and after the rear boundary, and for which the intensity clearly exceeds that of the variations in the background. Furthermore, for some of these 22 events, more than one peak is found. In Table 2 we list each of the 22 events that exhibit peaks in the proton density near the trailing edge of the MC. These are listed together with one or more possible explanations describing the presence of the density peaks.

## **5.1 Intrinsic Processes at the Sun**

We looked for the low coronal counterparts of each of the observed MCs in Table 2. To track an ICME back to the solar disc, we estimated the CME launch time by using the ICME leading-edge speed measured by ACE, which has been proven to be a better measurement for estimating travel times than the CME speed as derived from coronagraphs (Kilpua et al., 2012b), and considering a constant speed on the way from the Sun to 1 AU. To account for probable accelerations or decelerations of CMEs into the interplanetary space, we searched for the CME candidates within a three-day time window around the estimated CME launch time. In order to find the associated CMEs, we used the online LASCO CME catalogue ([http://cdaw.gsfc.nasa.gov/CME\\_list/](http://cdaw.gsfc.nasa.gov/CME_list/), Yashiro et al., 2004) and studied daily coronagraph movies as well as extreme ultraviolet movies from EIT observations. The identified lower coronal signatures are listed in Table 2 (last two columns). For some events data gaps, or multiple events occurring close in time did not allow to find an unambiguous link between a MC and a CME.

A possible cause of the density peak in the MC tail is an associated eruptive filament. If a filament eruption was observed in EIT (19.5 or/and 30.4 nm) observations within a few hours interval before the first appearance of the CME in LASCO C2 field of view, or if in the H $\alpha$  series of images we could see a filament which was clearly gone after the CME erupted, we consider it to be associated with the MC observations. Nevertheless, we encountered several difficulties in identifying the associated eruptive filaments: 1) As all the CMEs had their source regions close to the centre of the solar disc (and not on the limb), the erupting

filament was often difficult to identify within the bright surrounding solar features in the EIT 19.5 nm data; 2) The temporal cadence of EIT 30.4 nm and H $\alpha$  images was generally very low, and the erupting filament could then be easily missed, or in some cases it was not clear if the filament had really erupted or just disappeared from the bandpass (for example due to heating). Out of the events presenting a proton density peak near the MC trailing edge, only four could be unambiguously linked to a filament eruption at the Sun (indicated by “FIL” in the last column of Table 2). Hence, for the majority of the cases, the density peaks can hardly be explained by the presence of the filament material. This is in agreement with the results by Lepri et al. (2010), who showed that prominence material is normally found only in a very few ICMEs observed at 1 AU. Furthermore, Howard (2015) showed that the prominence mass can be seen to disappear progressively in heliospheric imager data while propagating away from the Sun (see Figure 7 in the paper by Howard, 2015). This might be due to the prominence material mixing with the surrounding solar wind, leaving little prominence plasma to be detected at 1 AU.

It should be noted that even without the presence of associated prominence material, the density enhancement could still be an intrinsic part of the MC created in the low corona. For example, dense loops encircling the erupting flux rope can become a part of it after reconnection (van Ballegoijen and Martens, 1989; Aulanier et al., 2010). The crossing of small-scale flux tubes with different densities within a single MC could be a plausible explanation. With the total pressure balance maintained, a density peak is expected to be associated with a decrease of the magnetic field magnitude (unless the plasma pressure remains the same due to lower temperature). Magnetic flux tubes with an origin different than that of their environment (e.g. high-density reconnected loops, see Dere et al. 1999) or the post-eruptive reconnection outflow proposed by Riley et al. (2002), could partially explain the density peaks in more than a half of the events in Table 2 (14 cases out of 22, indicated by “I” in column 6 of Table 2). We used the simultaneous increase of density and decrease of magnetic field magnitude as the criterion to mark the density peak as intrinsic (I) in Table 2. An example of such an event is shown in the left panels of Figure 4, corresponding to a MC from 6 November 2000. The density peaks right after the trailing edge of the MC, at the same time that the magnetic field intensity drops. As seen in the solar wind speed panel, there is no HSS trailing the MC. Furthermore there are three events (1999/02/18, 2000/02/12, 2006/08/30) where only an intrinsic explanation could explain the density peaks, as these MCs were neither followed by a high-speed stream nor did they show a strong expansion.

## 5.2 Compression by an Overtaking High-Speed Stream

The dynamic pressure exerted on a magnetic cloud by a HSS overtaking it could generate the compression necessary to produce a peak in proton density. By visual examination of

the events it was found that 17 cases of the total 22 showing rear density peaks have such a HSS trailing them. Figure 4 (right panel) shows an example of a MC from 22 July 2004 with a density peak just before its trailing edge followed by a HSS, which is clear from the comparison of the solar wind speed at the rear boundary of the MC with the speed of the solar wind trailing it. Table 2 (last column) indicates that out of 17 events with a trailing HSS, for 11 of them a coronal hole was present at the Sun, located to the east of the source region of the CME cases), the remaining cases (6 out of 17) have a data gap or the source could not be identified. Since coronal holes are the sources of fast solar wind, we conclude that they are the sources of the HSSs trailing the MCs and causing the density peaks at the rear boundaries of MCs.

For these events, a peak in magnetic field intensity should be expected too as a result of the compression. This peak is not visible in the superposed epoch analysis of Figure 2. Firstly, this is because these plots include all the MCs, in particular cases with an intrinsic density enhancement (corresponding partly to a weaker magnetic field). Furthermore, the magnetic field enhancement is frequently stacked with the enhanced field of the MC (this is different for the density, which is typically comparable inside and outside MCs). However, limiting the analysis to cases having a trailing HSS, we find an enhanced magnetic field for 12 out of 17 cases, comparable or larger than in the MC, associated with the peak density. An example is shown in the right panels of Figure 4 with an unusual peak of  $B$  present at the rear of the MC. It is associated with a positive gradient of plasma velocity and a density peak. Finally, the 5 remaining cases without increase in  $B$  correspond to weak HSS.

We would like to point out that, when using the *in situ* data, we only have a local snap shot of the cloud evolving in time. For example, an overtaking flow could interact with a MC close to the Sun, compressing the plasma at an early stage of its propagation and creating the density peak. This fast flow and the associated interaction could be mostly over at the time of the observations at 1 AU and therefore it would not be possible to associate the fast flow with the corresponding density peak. The opposite may also occur, i.e. the interaction takes place at the moment of observations at 1 AU, but without having a sufficient time to build a strong density enhancement. This indicates that a one-to-one association between the observed density peaks and their causes cannot always be expected.

### 5.3 Expansion

In general, magnetic clouds are expanding structures. Such expansion, when strong enough, could generate a peak in density close to the boundaries of the flux rope. Several MCs with rear proton density peaks also exhibit signatures of strong expansion. The dimensionless expansion rate  $\zeta$  (Gulisano et al., 2010), is shown for each cloud in Table 2. A positive value of the expansion factor indicates that the clouds are expanding. The left panels of Figure 4

show an example of a strongly expanding MC, with a distinct density increase just after the rear edge of the cloud.

Values of  $\zeta$  in the range  $\sim 0.8 - 1$  correspond to the expansion needed for the cloud to be in total pressure balance with the surrounding solar wind (Démoulin and Dasso, 2009). Higher values of  $\zeta$  may contribute to the creation of a density peak. We fix a threshold of 1 for  $\zeta$  to consider that the MC expansion may be a possible source for the density peak at the trailing edge of a MC. Table 2 shows that six MCs from the total of 22 events showing the rear density peaks have  $\zeta$  higher than 1, meaning that MC expansion could be at the origin of only 27% of events with the density peaks. Furthermore, from Table 2 it can be seen that there is no single event where the expansion can be the only cause for the density peaks, so we conclude that the expansion is not an efficient mechanism to form a density peak.

In summary, compression by trailing high speed streams (HSSs) seems to be the most promising explanation for the creation of the trailing density peaks in MCs. This mechanism, together with intrinsic processes corresponding to flux tubes with different plasma and magnetic field properties, could explain the majority of the observed peaks. A combination of the above effects could also explain why some MCs exhibit multiple density peaks in their tails. Out of 22 events, there were eight cases showing multiple proton density peaks (an example is shown in Figure 5). For some of them, a combination of effects (expansion, compression, intrinsic processes) is present, although it is not obvious if different processes will produce separate peaks.

MC Start (1)	MC End (2)	Number of trailing Peaks (3)	HSS (4)	$\zeta$ (5)	Trailing density peak origin (6)	Corresponding CME (7)	Solar features (8)
<b>1998</b>							
03/04 13:00	03/06 06:00	2	Y	0.69	O	02/28 12:48	CH
<b>1999</b>							
02/18 14:00	02/19 10:00	1	N	0.86	I	Data gap	
08/09 21:00	08/10 17:00	2	Y	0.43	I, O	NA	
<b>2000</b>							
02/12 17:00	02/13 00:00	1	N	0.01	I	02/10 02:30	
07/15 21:00	07/16 10:00	2	Y	1.88	E, I, O	07/14 10:54	CH, FIL
08/12 05:00	08/13 05:00	1	N	1.21	E, I	08/09 16:30	
11/06 22:00	11/07 18:00	1	N	1.77	E, I	11/03 18:26	
<b>2002</b>							

03/19 23:00	03/20 16:00	1	Y	0.79	O,I	03/15 23:06	CH
03/24 12:00	03/25 22:00	1	Y	0.60	O	03/20 17:06	CH
04/18 03:00	04/19 02:00	1	Y	0.62	O, I	04/15 03:50	CH
08/01 12:00	08/01 23:00	1	Y	0.69	O	07/29 23:30	CH, FIL
<b>2003</b>							
06/17 18:00	06/18 08:00	1	Y	0.34	O	06/14 01:54	CH, FIL
11/20 10:00	11/21 02:00	1	Y	1.14	E, I, O	11/18 08:50	CH, FIL
<b>2004</b>							
04/04 02:00	04/05 17:00	2	Y	0.82	O	Data gap	
07/22 15:00	07/23 01:00	1	Y	-3.88	O	07/20 13:31	CH
07/24 14:00	07/25 15:00	2	Y	1.27	E, O	07/22 07:31	CH
08/29 19:00	08/30 22:00	2	Y	0.47	I, O	NA	
<b>2005</b>							
05/20 07:00	05/21 05:00	1	Y	0.89	I, O	05/16 13:50	CH
06/15 05:00	06/16 09:00	2	Y	1.02	E, I, O	Data gap	
07/17 14:0	07/18 04:00	1	Y	0.86	O	NA	
12/31 13:00	01/01 11:00	1	Y	0.86	O, I	NA	
<b>2006</b>							
08/30 20:00	08/31 15:00	2	N	0.98	I	Data gap	

Table 2. Summary of the magnetic cloud events where a clear peak in density is seen close (within 30% of the cloud duration) to the rear boundary of the cloud. Columns 1 and 2 list the start and end times of the MCs (from the R&C list). Column 3 shows the number of trailing peaks identified. Column 4 states whether a high-speed stream (HSS) signature is present behind the cloud. Column 5 shows the dimensionless expansion rate  $\zeta$  defined by Gulisano et al. (2010), with positive values of this factor indicating that the cloud is expanding, and with the value  $\zeta = 1$  set as a threshold for considering expansion as a source for the rear density peak. Column 6 gives the probable origin of the rear proton density peak, where E indicates MC expansion, I indicates an intrinsic property of the plasma flow at or close to the Sun, and O stands for an overtaking flow. Column 7 details the date and time of the corresponding CME on the Sun, with “Data gap” corresponding to missing SOHO data (EIT and/or LASCO), and NA standing for the cases where no association with a solar counterpart could be found. Column 8 lists any related solar feature: CH means that a coronal hole was located east of the source region of the CME, FIL stands for a filament eruption clearly identified in relation to the CME.

## 6 Summary and Conclusions

In this work we present an analysis of the internal structure of MCs observed at 1 AU. We applied a superposed epoch method to 63 events detected by ACE at the L1 point, observed between 1998 and 2006. We obtained an ensemble profile for each plasma and magnetic field quantity, which represents an average at each point of the cloud over all the events. By performing such an analysis, we have identified several MC characteristics that were known

to be present in individual events, but can now be generalized to a large sample of MCs, as shown by the typical magnetic cloud profiles constructed in this study. They include:

- Proton density and temperature peak before the flux rope, that is a consequence of the hot and dense material accumulated there (MC sheath).
- The proton temperature and the plasma beta are low throughout the duration of the MC.
- The expansion of the cloud is marked by the negative slope of the speed profile and the low proton temperature.
- The  $O^{+7}/O^{+6}$  profile exhibits a clear enhancement throughout the duration of the MC, indicating high temperatures in the source region of the corresponding CME.
- The peak in the magnetic field magnitude inside magnetic clouds is not symmetric, which is a consequence of the combined effect of the MC expansion, a possible spatial asymmetry within the flux rope, and its asymmetric interaction with the surrounding solar wind.
- Magnetic field vector fluctuations, normalized to the mean field strength, are low throughout the duration of the MC, thus confirming that the low magnetic field variation can be considered as a very robust parameter for the identification of MC boundaries, which is also consistent with the analysis of ultra-low-frequency magnetic field fluctuations in MCs by Kilpua et al. (2013b).
- The intervals of decreased values of the plasma beta are also a very good proxy for the flux rope duration.

Furthermore, new insights into the internal characteristics of MCs were found in our analysis:

- Log-normal distribution function can be used to describe the distribution of plasma and magnetic field parameters near the center of MCs. This is in agreement with previous works that find log-normal distribution functions for parameters within ICMEs (Mitsakou and Moussas, 2014; Guo et al., 2010), and in the solar wind at 1 AU (Burlaga and Lazarus, 2000 and references therein). Such distributions are believed to indicate a consequence of the presence of non-linear multiplicative processes (e.g. Montroll and Shlesinger, 1982).
- The  $O^{+7}/O^{+6}$ , and the alpha-to-proton number density ratio (two parameters that characterize the flux rope when it was much closer to the Sun than 1 AU), present typical ICME values for a period extended well beyond the defined flux rope rear boundary, a result consistent with the reconnection between the flux rope and the magnetic field of the ambient solar wind. In particular, the  $O^{+7}/O^{+6}$  values show a slower recovery rate to background solar wind levels at the MC rear compared to the fast rise rate at the MC front. This could be an indication of the presence of a long back region in magnetic clouds. Then, the typical MC should be eroded at 1 AU. This

is an important result since studies focusing on the characteristics of MCs and in particular the magnetic field structure should take the erosion process into account, for example in the flux rope fitting procedure (e.g., Lavraud et al. 2014; Ruffenach et al., 2015).

- There are proton density peaks observed around the trailing edge of a significant fraction of the studied MCs (22 out of 63). For 17 of these 22 events, there was evidence of a trailing fast-stream compressing the cloud, while 6 events showed strong internal expansion, and 4 events were associated with a filament at the Sun. The overtaking fast flows scenario is sufficient to explain most of the observed proton density peaks. Finally, proton density increases could also be attributed to other intrinsic processes occurring close to the Sun (the plasma structure of magnetic loops in the erupting region, reconnection outflows, etc.).
- Some events present more than one proton density peak in the MC tail, which may be a further indication of multiple processes creating the density enhancement.

## Acknowledgements

L. R. and A. N. Z. acknowledge support from the Belgian Federal Science Policy Office through the ESA-PRODEX program. Luciano Rodriguez acknowledges support from the European Union Seventh Framework Programme (FP7/2007-2013) under grant agreement number 263252 (COMESSEP). SOHO is a project of international cooperation between ESA and NASA. This research has been partially funded by the Interuniversity Attraction Poles Programme initiated by the Belgian Science Policy Office (IAP P7/08 CHARM). This work was partially supported by Argentinean grant UBACyT 20020120100220, PICT-2013-1462, PIP-11220130100439CO (CONICET), PIDDEF 2014-2017 Nro. 8, and by the Argentina-Belgium agreement between the FNRS Belgium (V4/325 M) and MINCyT Argentina (BE/13/07). This work was also partially supported by a 1 month invitation of P.D. to the Instituto de Astronomía y Física del Espacio, and by a 1 month invitation of S.D. to the Observatoire de Paris. S.D. is member of the Carrera del Investigador Científico, CONICET. E. K. acknowledges support from Academy of Finland project 1267087.

## References

- Aulanier, G., Török, T., Démoulin, P., DeLuca, E.E.: 2010, *Astrophys. J.* 708, 314.
- Billings, D.E.: 1966, *A guide to the solar corona*, New York Academic Press, New York.

Borovsky, J.E., Thomsen, M.F., Elphic, R.C.: 1998, *J. Geophys. Res.* 103, 17617.

Brueckner, G.E., Howard, R.A., Koomen, M.J., Korendyke, C.M., Michels, D.J., Moses, J.D., Socker, D.G., Dere, K.P., Lamy, P.L., Llebaria, A., Bout, M.V., Schwenn, R., Simnett, G.M., Bedford, D.K., Eyles, C.J.: 1995, *Solar Phys.* 162, 357.

Burlaga, L.F.: 1991, *Physics and Chemistry in Space* 21, 1.

Burlaga, L.F., Lazarus, A.J.: 2000, *J. Geophys. Res.* 105, 2357.

Burlaga, L.F., Fitzenreiter, R., Lepping, R., Ogilvie, K., Szabo, A., Lazarus, A., Steinberg, J., Gloeckler, G., Howard, R., Michels, D., Farrugia, C., Lin, R.P., Larson, D.E.: 1998, *J. Geophys. Res.* 103, 277.

Burlaga, L., Sittler, E., Mariani, F., and Schwenn, R.: 1981, *J. Geophys. Res.* 86, 6673.

Dasso, S., Mandrini, C.H., Démoulin, P., Luoni, M.L.: 2006, *Astron. Astrophys.* 455, 349.

Dasso, S., Nakwacki, M.S., Démoulin, P., Mandrini, C.H.: 2007, *Solar Phys.* 244, 115.

Davis, C.J., Davies, J.A., Lockwood, M., Rouillard, A.P., Eyles, C.J., Harrison, R.A.: 2009, *Geophys. Res. Lett.* 36, 8102.

Delaboudinière, J.P., Artzner, G.E., Brunaud, J., Gabriel, A.H., Hochedez, J.F., Millier, F., et al.: 1995, *Sol. Phys.* 162, 291.

Démoulin, P., Dasso, S.: 2009, *Astron. Astrophys.* 498, 551.

Démoulin, P., Nakwacki, M.S., Dasso, S., Mandrini, C.H.: 2008, *Solar Phys.* 250, 347.

Démoulin, P., Janvier, M., Dasso, S.: 2015, submitted to *Astron. Astrophys.*

Dere, K.P., Brueckner, G.E., Howard, R.A., Michels, D.J., Delaboudinière, J.P.: 1999, *Astrophys. J.* 516, 465.

Fenrich, F.R., Luhmann, J.G.: 1998, *Geophys. Res. Lett.* 25, 2999.

Gosling, J.T.: 1990, Washington DC American Geophysical Union Geophysical Monograph Series 58, 343.

Gosling, J.T., Pizzo, V., Bame, S.J.: 1973, *J. Geophys. Res.* 78, 2001.

Gosling, J.T., Riley, P., McComas, D.J., Pizzo, V.J.: 1998, *J. Geophys. Res.* 103, 1941.

Gulisano, A.M., Démoulin, P., Dasso, S., Ruiz, M.E., Marsch, E.: 2010, *Astron. Astrophys.* 509, A39.

Guo, J., Feng, X., Zhang, J., Zuo, P., Xiang, C.: 2010, *J. Geophys. Res.* 115, 9107.

Henke, T., Woch, J., Mall, U., Livi, S., Wilken, B., Schwenn, R., Gloeckler, G., von Steiger, R., Forsyth, R.J., Balogh, A.: 1998, *Geophys. Res. Lett.* 25, 3465.

Howard, T.A.: 2015, *Astrophys. J.* 806, 175.

Howard, T.A., Nandy, D., Koepke, A.C.: 2008, *J. Geophys. Res.* 113, 1104.

Hundhausen, A.J., Gilbert, H.E., Bame, S.J.: 1968, *Astrophys. J.* 152, L3.

Illing, R.M.E., Hundhausen, A.J.: 1986, *J. Geophys. Res.* 91, 10951.

Kilpua, E.K.J., Mierla, M., Rodriguez, L., Zhukov, A.N., Srivastava, N., West, M.J.: 2012a, *Solar Phys.* 279, 477.

Kilpua, E.K.J., Li, Y., Luhmann, J.G., Jian, L.K., Russell, C.T.: 2012b, *Ann. Geophys.* 30, 1037.

Kilpua, E.K.J., Hietala, H., Koskinen, H.E.J., Fontaine, D., Turc, L.: 2013a, *Ann. Geophys.* 31, 1559.

Kilpua, E.K.J., Isavnin, A., Vourlidas, A., Koskinen, H.E.J., Rodriguez, L.: 2013b, *Ann. Geophys.* 31, 1251.

Klein, L.W., Burlaga, L.F.: 1982, *J. Geophys. Res.* 87, 613.

Lavraud, B., Denton, M.H., Thomsen, M.F., Borovsky, J.E., Friedel, R.H.W.: 2005, *Ann. Geophys.* 23, 2519.

Lavraud, B., Ruffenach, A., Rouillard, A. P., Kajdic, P., Manchester, W.B., Lugaz, N.: 2014, *J. Geophys. Res.* 119, 26.

Lepping, R.P., Berdichevsky, D.B., Ferguson, T.J.: 2003, *J. Geophys. Res.* 108, 1356.

Lepri, S.T., Zurbuchen, T.H.: 2010, *Astrophys. J. Lett.* 723, L22.

Lepri, S.T., Zurbuchen, T.H., Gruesbeck, J.R., Gilbert, J.A.: 2014, in Schmieder, B., Malherbe, J.-M., Wu, S.T. (eds.), *IAU Symposium 300*, 289.

Lynch, B.J., Zurbuchen, T.H., Fisk, L.A., Antiochos, S.K.: 2003, *J. Geophys. Res.* 108, A01239.

Manchester, W.B., Kozyra, J.U., Lepri, S.T., Lavraud, B.: 2014, *J. Geophys. Res.* 119, 5449.

Masías-Meza J.J., Dasso S., Demoulin P., Rodriguez L., Janvier M.: 2016, *Astron. and Astrophys.*, in preparation.

Mitsakou, E., Moussas, X.: 2014, *Solar Phys.* 289, 3137.

Montroll, E.W., Shlesinger, M.F.: 1982, *Proc. Natl. Acad. Sci.* 79, 3380.

- Möstl, C., Farrugia, C.J., Temmer, M., Miklenic, C., Veronig, A.M., Galvin, A.B., Leitner, M., Biernat, H.K.: 2009, *Astrophys. J. Lett.* 705, L180.
- Ontiveros, V., Vourlidas, A.: 2009, *Astrophys. J.* 693, 267.
- Reeves, G.D., Friedel, R.H.W., Belian, R.D., Meier, M.M., Henderson, M.G., Onsager, T., Singer, H.J., Baker, D.N., Li, X., Blake, J.B.: 1998, *J. Geophys. Res.* 103, 17559.
- Richardson, I.G., Cane, H.V.: 1995, *J. Geophys. Res.* 100, 23397.
- Richardson, I.G., Cane, H.V.: 2004, *J. Geophys. Res.* 109, 9104.
- Richardson, I.G., Cane, H.V.: 2010, *Solar Phys.* 264, 189.
- Riley, P., Linker, J.A., Mikić, Z., Odstrcil, D., Pizzo, V.J., Webb, D.F.: 2002, *Astrophys. J.* 578, 972.
- Rodriguez, L., Woch, J., Krupp, N., Fränz, M., von Steiger, R., Forsyth, R.J., Reisenfeld, D.B., Glaßmeier, K.-H.: 2004, *J. Geophys. Res.* 109, 1108.
- Rodriguez, L., Mierla, M., Zhukov, A.N., West, M., Kilpua, E.: 2011, *Solar Phys.* 270, 561.
- Ruffenach, A., Lavraud, B., Farrugia, C.J., Démoulin, P., Dasso, S., Owens, M.J., Sauvaud, J.-A., Rouillard, A.P., Lynnyk, A., Foullon, C., Savani, N.P., Luhmann, J.G., Galvin, A.B.: 2015, *J. Geophys. Res.* 120, 43.
- Schwenn, R., Rosenbauer, H., Muehlhaeuser, K.-H.: 1980, *Geophys. Res. Lett.* 7, 201.
- Song, H. Q., Chen, Y., Zhang, J., Cheng, X., Wang, B., Hu, Q., Li, G., Wang, Y.M.: 2015, *Astrophys. J. Lett.* 808, L15.
- van Ballegooijen, A.A., Martens, P.C.H.: 1989, *Astrophys. J.* 343, 971.
- Vourlidas, A., Lynch, B.J., Howard, R.A., Li, Y.: 2013, *Solar Phys.* 284, 179.
- Wang, C.-P., Lyons, L.R., Angelopoulos, V., Larson, D., McFadden, J.P., Frey, S., Auster, H.-U., Magnes, W.: 2008, *Geophys. Res. Lett.* 35, 17.
- Yashiro, S., Gopalswamy, N., Michalek, G., St.Cyr, O.C., Plunkett, S.P., Rich, N.B., Howard, R.A.: 2004, *J. Geophys. Res.* 109, A07105.

## Figures

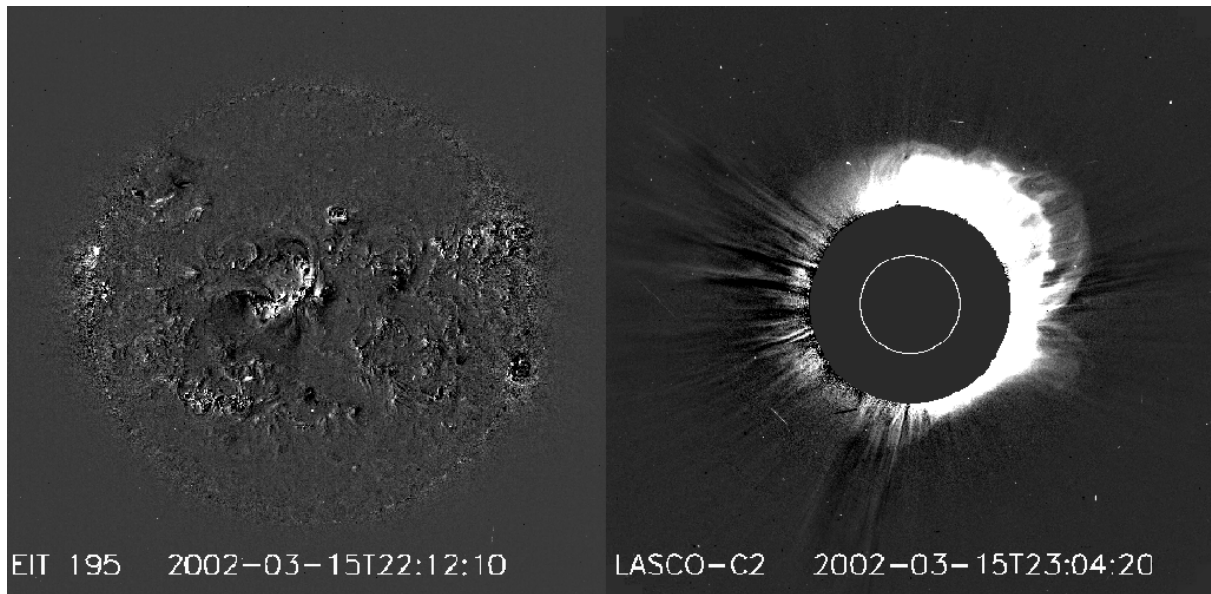


Figure 1. CME of 15 March 2002. Observed as a full halo by SOHO LASCO-C2 (right panel). The corresponding eruption is seen in the source region NOAA AR 9866 close to disc center, as captured by SOHO EIT (left panel). Both are running difference images, where the previous image is subtracted from the current one.

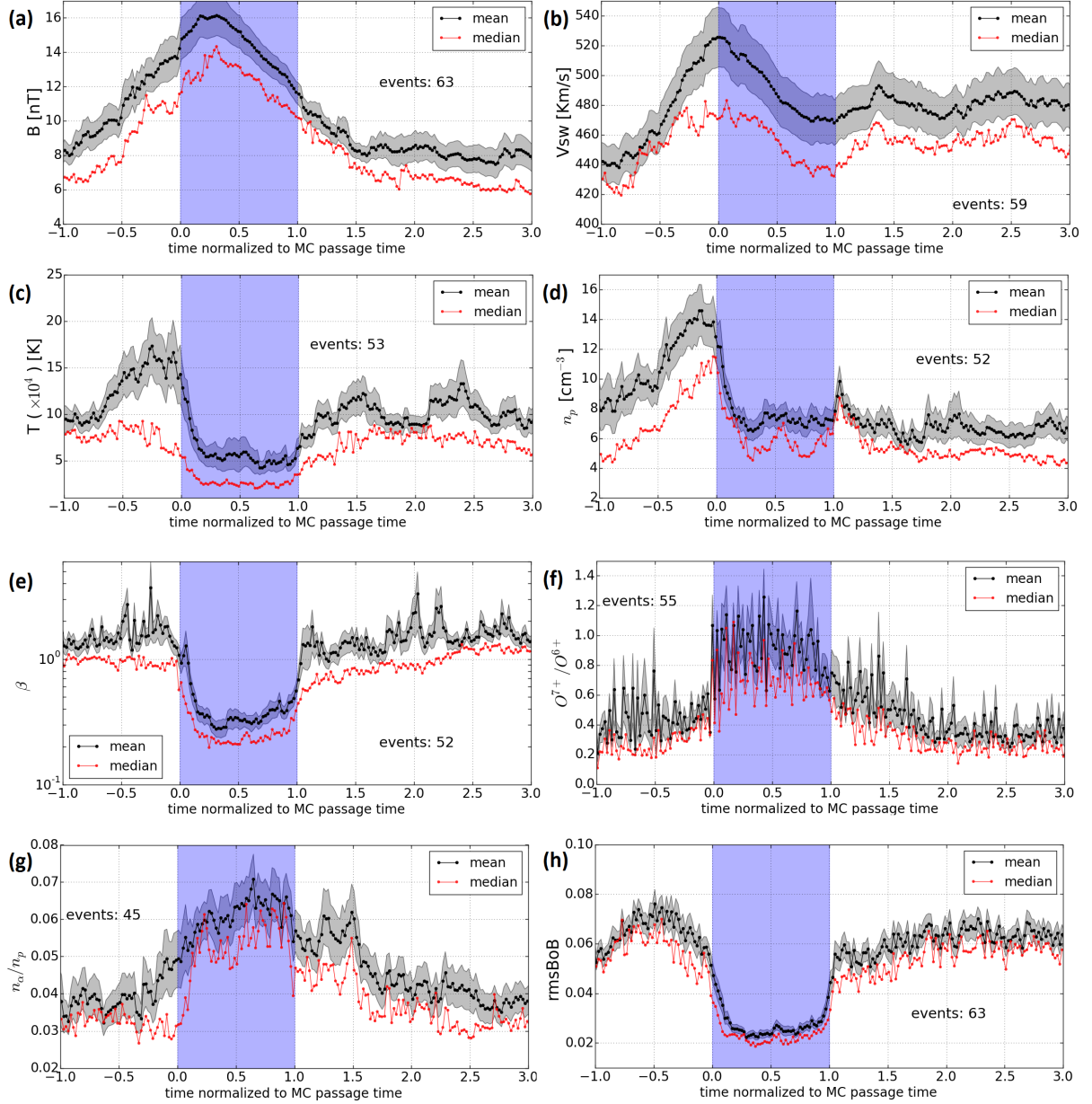


Figure 2. Superposed epoch profiles of plasma and magnetic field characteristics measured by ACE for the magnetic clouds of our list. Each plot was created by applying a superposed epoch method to 63 MCs. Events with a data gap larger than 20 % were not used in the analysis. Since the number of data gaps varied between individual instruments, the number of MCs used varied for each parameter (see the number of considered events inside each panel). Panels reading left to right and top to bottom are (a) interplanetary magnetic field intensity, (b) solar wind speed, (c) proton temperature, (d) proton number density, (e) plasma beta, (f)  $O^{+7}/O^{+6}$  relative abundance, (g) alpha-to-proton number density ratio and (h) normalized magnetic field vector variance. MC periods are marked by the blue areas. Error bars (in grey) represent the standard deviations of the mean (black curve), and the red curve is the median.

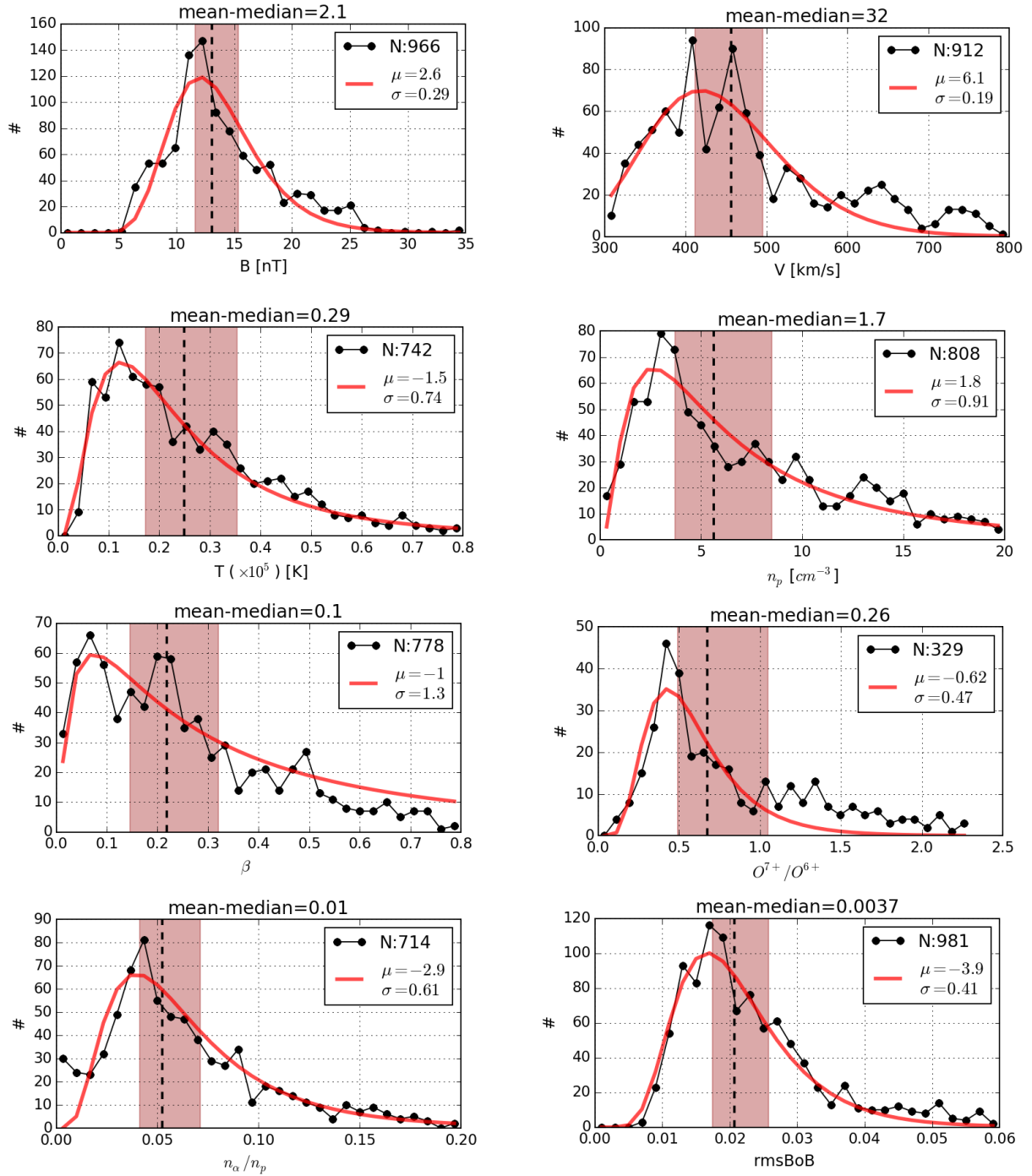


Figure 3. Probability distribution functions of the plasma and magnetic field parameters presented in Figure 2 for our dataset of magnetic clouds (taken from the center of the MCs).  $N$  indicates the number of points used in the distribution shown, the red line is the log-normal fit derived using the parameters  $\mu$  and  $\sigma$  of the distribution function (see Equation 3). The median value is indicated as a vertical dashed line. The red shadowed rectangle marks the area between the inferior and the superior percentile of the data ( $50-33/2 = 33.5\%$  and  $50+33/2 = 66.5\%$  of the maximum of the cumulative distribution function), to show the spreading of each observable in the distribution.

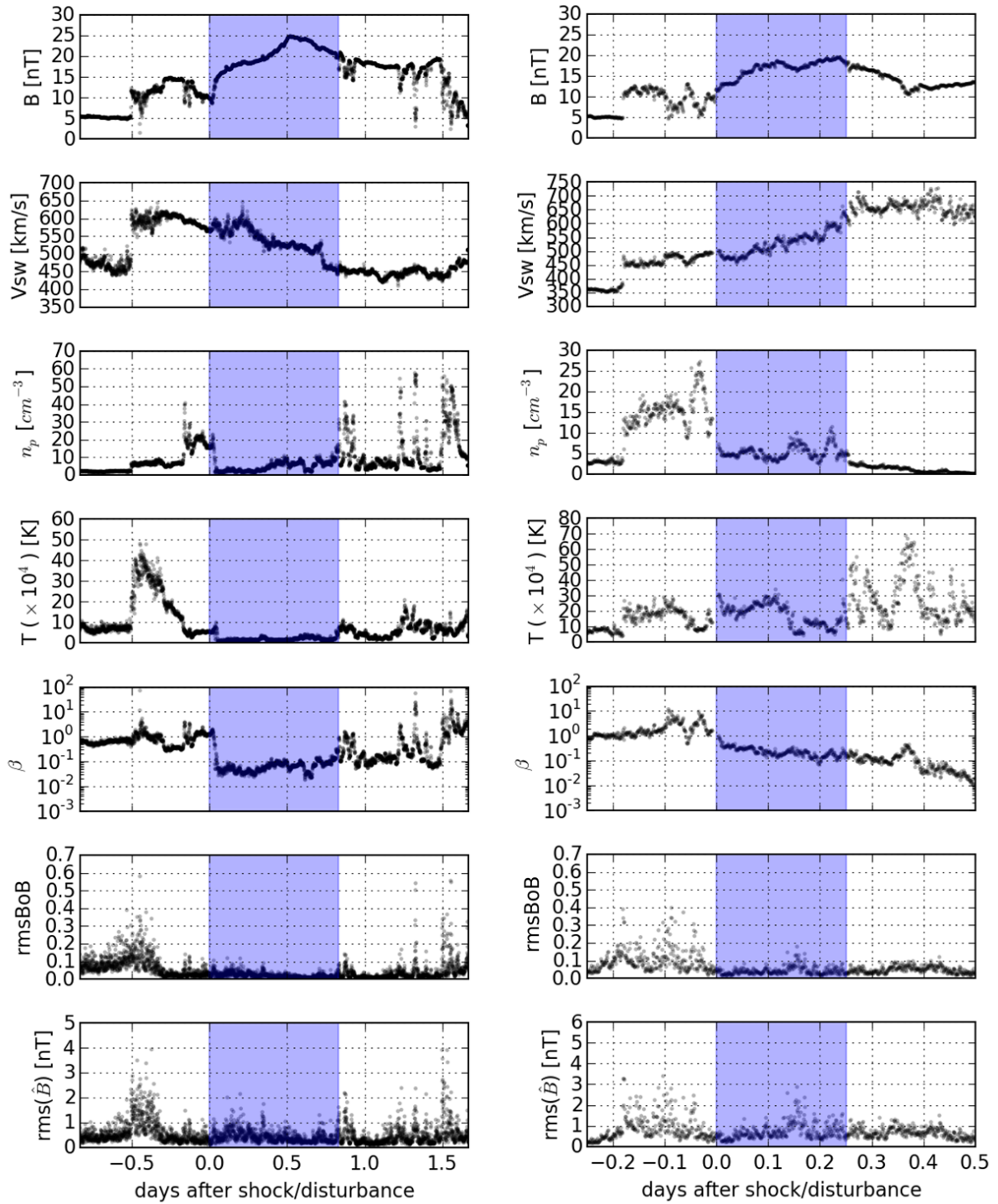


Figure 4. Examples of individual profiles of plasma and magnetic field parameters in two magnetic clouds. The panels from top to bottom are interplanetary magnetic field intensity, solar wind speed, proton number density, proton temperature, plasma beta, normalized and un-normalized magnetic field vector variance. The blue regions refer to the magnetic cloud passage. Left: the event on 6 November 2000, for which the causes of the plasma density peak at the cloud trailing edge are

plausibly the expansion of the cloud and an intrinsic structure found exactly after the rear boundary of the cloud. Right: the event on 22 July 2004, for which a fast stream, seen in the velocity profile right after the magnetic cloud, could be the cause of the density peak seen inside the flux rope, close to its rear boundary.

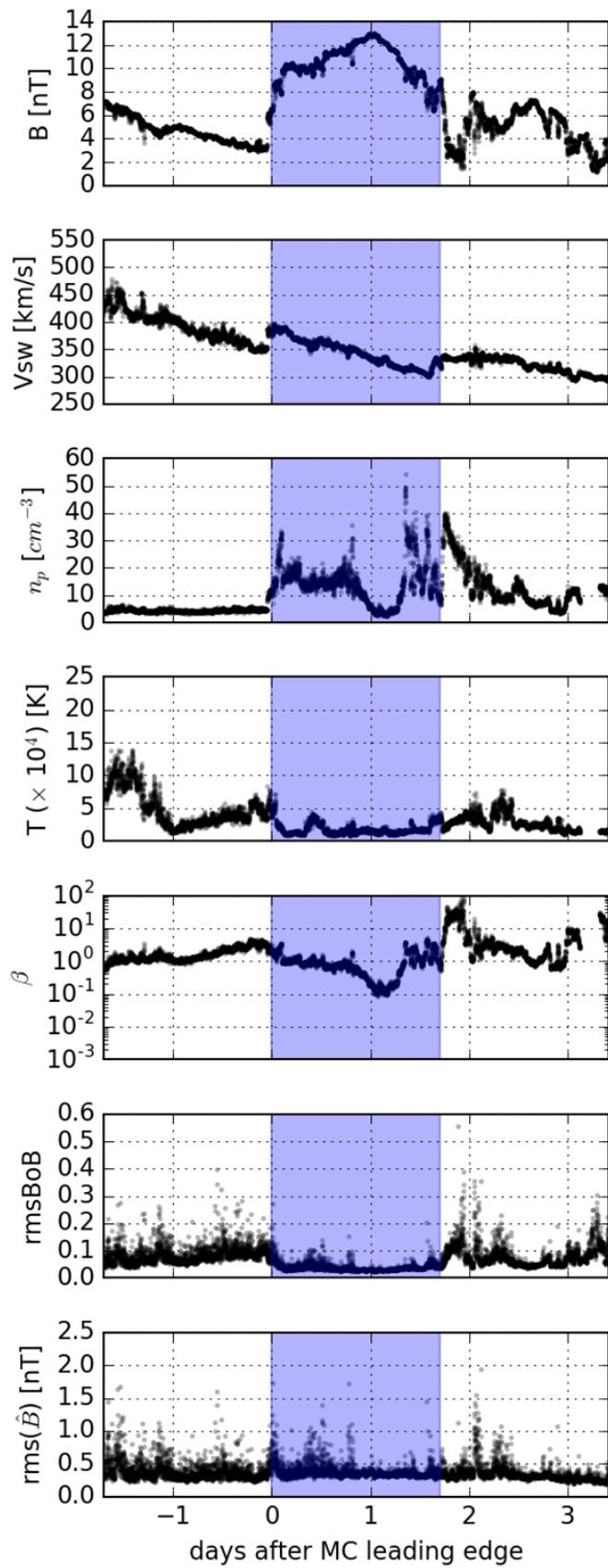


Figure 5. Example of a MC (1998/03/04) where multiple peaks are seen close to the rear boundary of the MC. The format is the same as in figure 4.

